Energy & Environmental Science

ROYAL SOCIETY OF CHEMISTRY

PAPER

View Article Online
View Journal

Cite this: DOI: 10.1039/d6ee02022d

Spider dragline silk-inspired 3D printed sustainable zinc ion batteries with ultrahigh stability

Hongyu Lu,†[a] Jisong Hu,†[b] Botao Jiang,†[c] Kaiqi Zhang,[a] Zhengyu Ju,[d] Gehong Su,*[e] Yuanyuan Gao,[a] Zhaodan Fu,[e] Jingxin Zhao,*[f] Bingang Xu*[a] and Guihua Yu*[d]

Aqueous zinc-ion batteries have garnered considerable attention in the field of large-scale energy storage due to their low cost, inherent safety, and environmental friendliness. Nevertheless, the issues of uncontrollable dendrite growth and hydrogen evolution reaction encountered by Zn metal anodes during cycling trigger electrode structural failure and lifespan decay, severely impeding their commercialization process. Here, we utilize a green process to extract recovered alginate (rSA) from waste algae and obtain a hydrogel carrier (rSP) with high ionic conductivity through one-step crosslinking. Inspired by the bionic structure of spider silk, rSP was combined with an MXene conductive network to directly fabricate a dual-network Zn anode (rSP/MXene/ZP) *via* multi-band UV 3D printing technology. Integrated experimental and theoretical analyses reveal that the cross-linking of rSP ensures the formation of a polyoxygen coordination network to create fast ion-conducting pathways, while simultaneously establishing multiple hydrogen bonds to constitute a dynamic cross-linking network. Consequently, symmetrical cells achieve exceptional cycling stability over 3000 h. The rSP/MXene/ZP anode is compatible with organic cathode materials (G-PAQS), and the assembled Zn-organic cell exhibits enhanced electrochemical performance and superior stability over 10 560 cycles.

Received 30th March 2026,
Accepted 26th May 2026

DOI: 10.1039/d6ee02022d

rsc.li/ees

Broader context

Aqueous zinc-ion batteries (AZIBs) are regarded as an ideal candidate for next-generation large-scale energy storage owing to their low cost, intrinsic safety, and environmental friendliness. However, severe side reactions and dendrite growth induced by interfacial concentration gradients seriously restrict the reversibility and cycling stability of Zn metal anodes. Herein, a bioinspired sustainable strategy is proposed to convert waste algae into high-performance anode materials through a fully green process, and a dual-network Zn metal anode (rSP/MXene/ZP) is directly fabricated *via* multi-band UV 3D printing. Within this anode, rSP crosslinking forms a polyoxygen coordination network to establish fast ion-conducting pathways, while simultaneously creating multiple hydrogen bonds to constitute a dynamic crosslinking network. The rSP/MXene/ZP anode is compatible with organic cathodes (G-PAQS), and the assembled Zn-ion cell delivers an ultralong cycle life with 92.4% capacity retention after 10 560 cycles at 4 A g^{-1}. More importantly, the anode can be recycled and reused after cell operation, further realizing the green circular-economy value of algae waste. This study demonstrates the sustainable potential of renewable biopolymers as Zn anode carriers, offering a viable pathway for developing eco-friendly Zn-ion batteries from abundant materials *via* sustainable processes.

[a] *Nanotechnology Center, School of Fashion and Textiles, The Hong Kong Polytechnic University, Hung Hom, Kowloon, Hong Kong 999077, P. R. China. E-mail: tcxubg@polyu.edu.hk*
[b] *Advanced Materials and Devices Laboratory, School of Materials Science and Engineering, School of Chemistry and Environmental Engineering, Hanshan Normal University, Chaozhou, 521041, P. R. China*
[c] *Department of Materials Science and Engineering, City University of Hong Kong, Hong Kong 999077, P. R. China*
[d] *Materials Science and Engineering Program and Walker Department of Mechanical Engineering, The University of Texas at Austin, Austin, TX, 78712, USA*
[e] *College of Science, Sichuan Agricultural University, Ya'an, 625014, P. R. China*
[f] *Key Laboratory of Low Dimensional Materials and Application Technology of Ministry of Education, School of Materials Science and Engineering, Xiangtan University, Xiangtan, 411105, P. R. China*
† These authors contributed equally to this work.

Introduction

Spider silk stands as one of the most exquisite structural materials in nature due to its high strength, high toughness, and high Young's modulus. Its toughness is superior to that of many synthetic fibers, such as nylon-66, Kevlar, and carbon fiber.[1] As the most promising type of spider silk for engineering applications, the large ampulla dragline silk plays a crucial role in the ecological behavior of spiders, including predation, movement, individual protection, and reproductive activities. Its outstanding mechanical properties are mainly reflected in its excellent energy dissipation capability, vibration damping characteristics, strain-hardening behavior, and superior dynamic mechanical properties.[2,3] The hierarchical structure of major ampullate dragline silk consists of periodically arranged crystalline and amorphous regions. Peptide molecules are connected by β-microcrystals to form a molecular network, and the internal multiscale hierarchical network structure achieves the unification of lightweight, ultra-high strength, toughness, and environmental stability. By mimicking the hierarchical network structure across molecular, nanoscale, and microscale levels, the toughness and environmental stability of materials can be enhanced simultaneously. This bioinspired design, which translates the structural principles of the most durable natural materials into a method for constructing high-performance conductive hydrogel hierarchical network structures as electrode carriers, is expected to expand its application scope in aqueous zinc-based energy storage systems and improve reliability in complex environments.

Aqueous Zn-based cells with Zn metal as the anode are emerging eco-friendly energy storage solutions (such as Zn-ion, Zn–air, and Zn-based flow cells), which exhibit compelling advantages including the abundant natural resources of low-cost Zn, inherent safety with the use of non-flammable aqueous electrolytes, low environmental risk, and high energy density. Specifically, Zn-ion batteries excel in terms of high power density and flexibility for portable electronics, Zn–air batteries offer ultrahigh energy density for long-duration storage, and Zn-based flow batteries enable decoupled energy/power scaling with extended cycling life for grid-scale applications.[4–6] These characteristics make them particularly suitable for applications in grid-scale storage systems. However, the uncontrollable dendrite growth and severe hydrogen evolution reaction (HER) occurring on the Zn metal anode surface induce electrode structural instability and significant cycling life degradation, which constitute a critical bottleneck hindering their practical implementation. Several innovative strategies have been proposed to inhibit the growth of Zn dendrites on the surface of Zn metal anodes, encompassing the design of the three-dimensional (3D) host, the establishment of artificial interfaces, and the modification of separators.[7–10] However, these strategies only inhibit the growth of dendrites through external physical/chemical treatments, rather than address the root cause of the dendrite formation. Another effective strategy involves utilizing soft substrate composite materials to release the stress during Zn deposition for dendrite suppression. However, such materials generally suffer from low conductivity and are prone to detachment due to mechanical mismatch during cycling. Although the incorporation of conductive two-dimensional (2D) materials can inhibit vertical dendrite growth through lattice matching and provide electronic conduction, conventional methods fail to achieve uniform distribution of 2D materials within the protective layer.[11] Moreover, the ion transport efficiency of the composite protective layer remains limited, constraining the full exploitation of the epitaxial inhibition mechanism. Therefore, the synergistic optimization of electronic/ionic conduction and mechanical stability at the Zn anode interface remains a critical challenge for advancing the commercial application of Zn metal anodes.

Inspired by the distinctive structure and properties of the large ampulla dragline silk, this article demonstrates a green quasi-solid ion/electron conductive cross-linked network. It ingeniously constructs an ion conductive network (rSP network) using sodium alginate derived from recycled seaweed waste (rSA) and cross-linked hydrogel with polyacrylamide (PAAm), while introducing 2D conductive material MXene as the electronic conductive network with Zn powder (ZP) as the Zn metal source. By utilizing multi-band UV 3D printing technology, two types of networks can be rapidly constructed, resulting in a dual-network Zn anode (rSP/MXene/ZP). By virtue of its internal ion/electron dual-network synergistic suppression mechanism, the prepared dual-network ZP anode can alleviate the side effects of the Zn metal anode in the cycling process. As expected, the rSP/MXene/ZP anode delivers long-term lifespans of 3000 h (at 2 mA cm^{-2} and 1 mAh cm^{-2}) and 750 h (at 10 mA cm^{-2} and 5 mAh cm^{-2}), respectively. Even under an ultra-high depth of discharge (DOD) of 88.5%, excellent cycling stability of 180 h can also be realized. Furthermore, as demonstrated in rSP/MXene/ZP//G-PAQS full cells, ultra-stable long-term cycling stability can be achieved, retaining 92.4% of its capacity at a current density of 4 A g^{-1} after 10 560 cycles. More importantly, the rSP/MXene/ZP Zn anode could be recycled and reused after cell operation which further realizes the green energy circular economy value of algae waste. The regenerated rSP/MXene/ZP anode was reassembled into a full cell with G-PAQS, demonstrating excellent cycling stability with 94.1% capacity retention after 5220 cycles at a current density of 4 A g^{-1}. This study emphasizes the sustainable utilization potential of recycling renewable biopolymers as carriers for Zn metal anodes, presenting a viable path for developing eco-friendly Zn ion batteries that are produced from abundant materials and manufactured using sustainable processes.

Results and discussion

Preparation and investigation of the bionic dual-network Zn metal anode

The fabrication process of the biomimetic dual-network Zn metal anode includes the recycling of waste seaweed and the integrated 3D printing of the biomimetic dual-network Zn metal anode. As shown in Fig. 1a, waste seaweed mainly includes kelp, enteromorpha and sargassum, all sourced from

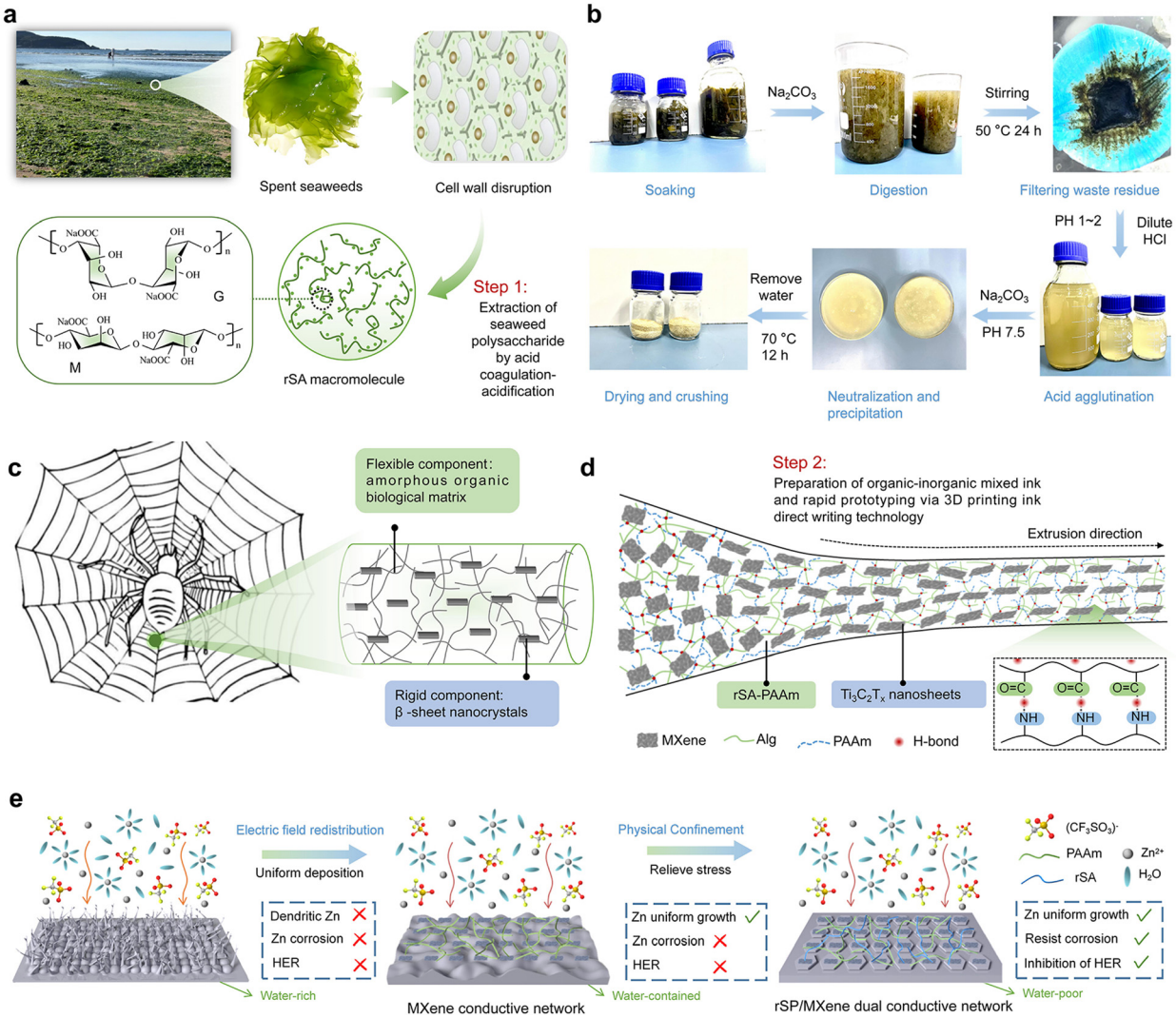

Fig. 1 Design concept of the dual-network rSP/MXene/ZP anode. (a) Schematic diagram of the waste seaweed recycle process. (b) Optical photographs of the extraction process of rSA. (c) Structure and composition of spider silk. (d) rSP/MXene dual-network conductive carrier inspired by the bionic structure of spider silk. (e) Inhibition mechanism of the rSP/MXene dual-network conductive carrier on Zn dendrite.

the Yellow Sea coast of China, and alginate was extracted from seaweed by acid coagulation (details are provided in the Methods section). Specifically, seaweed was soaked, chopped, and subjected to alkali digestion to generate sodium alginate solution, followed by hydrochloric acid acidification (pH 1–2) to precipitate alginic acid, neutralization and redissolution with sodium carbonate solution, and finally ethanol precipitation, filtration, and drying to obtain the recovered sodium alginate product (Fig. 1b). In addition, spider silk is renowned for its biphase structure: β-sheet nanocrystals rich in hydrogen bonds (rigid phase for strength enhancement) and an amorphous organic matrix (flexible phase for toughness), which collectively impart high strength and toughness with a clear structure–property relationship (Fig. 1c). Inspired by this structure, we introduced acrylamide (Am) chains into the recycled rSA biopolymer and incorporated rigid-structured MXene nanosheets to simulate the amorphous organic biological matrix and β-sheet nanocrystals, respectively. To facilitate the fabrication of these biomimetic dual-network Zn metal anodes, we developed a rapid printing manufacturing method based on multi-component ink by using 3D printing technology. The ink consists of sodium alginate, acrylamide and MXene nanosheets. By carefully controlling the printing parameters and the rheological properties of the ink, as well as utilizing the shearing force during the printing process, the MXene nanosheets are directionally arranged while other components (such as rSA and Am) are coordinately aligned in the ink. In the process of printing, the hydrogen bond crosslinking between carboxyl groups in rSA and amide groups in Am is formed by a simple and economical one-pot photo-initiated copolymerization, resulting in the crosslinked biomass copolymer rSP (Fig. 1d). This unique chemical crosslinking mechanism not only enhances the mechanical properties of the material but also optimizes its internal ion transport channels and electron conduction paths. The electronic conductive network created by MXene evenly distributes the electric field, preventing the tip

effect caused by an excessive local electric field and facilitating Zn ions to uniformly nucleate and grow on the electrode surface. The ionic conductive network rSP exhibits excellent elasticity and flexibility, which allows it to provide some space for deformation when the ZP expands in volume, thus effectively alleviating the internal stress caused by the growth of Zn dendrites (Fig. 1e).

The multi-band UV 3D printing process of the composite dual-network Zn metal anode is illustrated in Fig. 2a and Fig. S1. The process begins with the blending of the organic–inorganic ink, where the crosslinking of rSA with PAAm and the directional alignment of MXene nanosheets endow the dual-network matrix with good electrical conductivity and flexibility. A single layer of $Ti_3C_2T_x$ MXene sheets was exfoliated using an etching method. XRD patterns are depicted in Fig. S2, where $Ti_3C_2T_x$ MXene exhibits good crystallinity and purity, with its characteristic peak at 6.56° attributed to the (002) crystal plane. This indicates that MXene has been successfully synthesized and confirms the existence of a layered structure. In addition, the hexagonal close packing (hcp) crystal structure of ZP was identified by indexing peaks at 36.2° for the (002) plane, 43.5° for the (101) plane, and 54.3° for the (102) plane (JCPDS No. 04-0831). Due to the strong Zn signal and the small amount of $Ti_3C_2T_x$ MXene, only the weak (002) plane of the $Ti_3C_2T_x$ MXene pattern was detected in the MXene/ZP composite. Transmission electron microscopy (TEM) images (Fig. S3) show that $Ti_3C_2T_x$ nanosheets are transparent and folded into a 2D sheet structure, with lateral dimensions of about 1–3 μm.

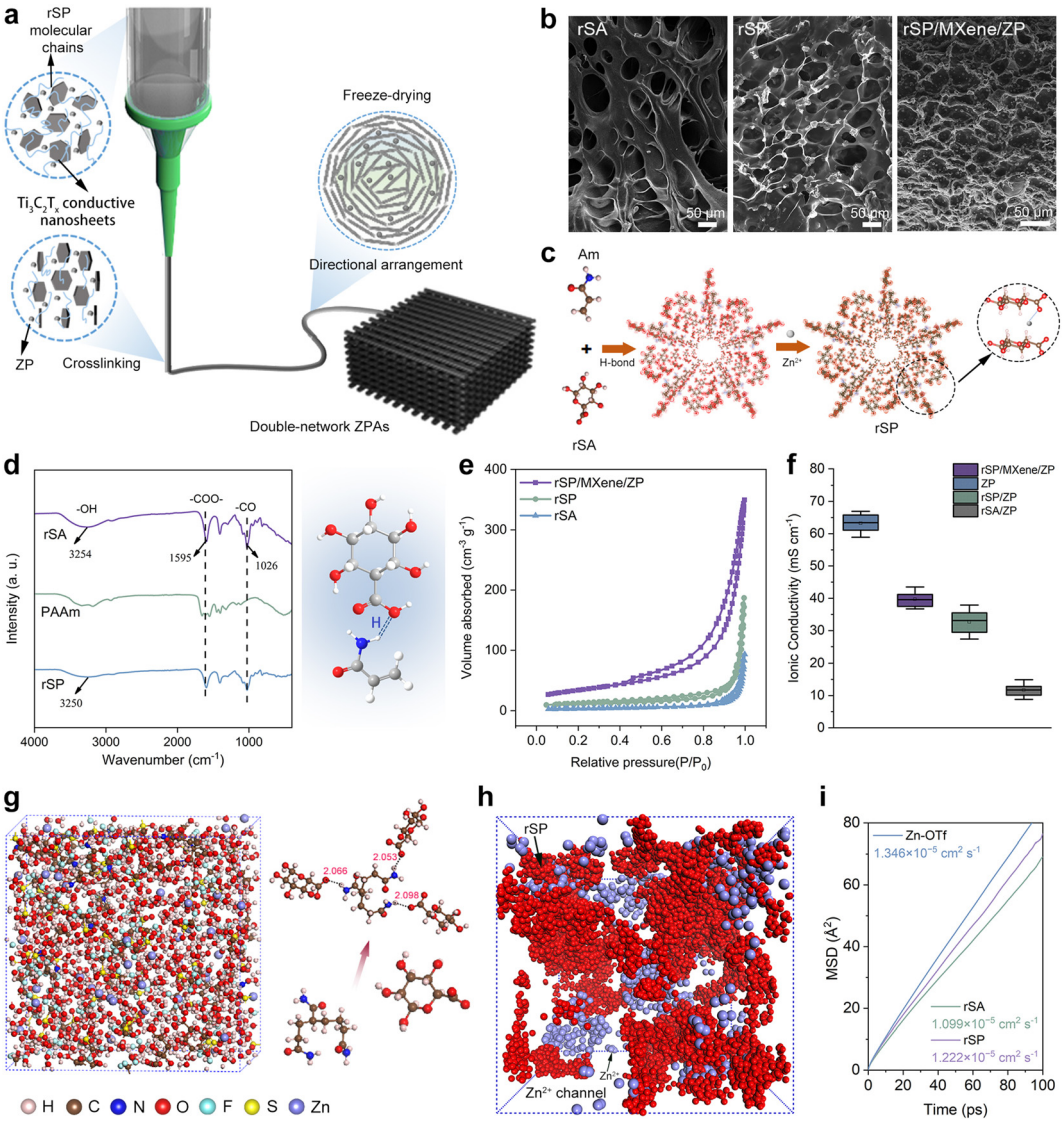

Fig. 2 Fabrication and structural characterization of rSP/MXene/ZP. (a) Illustration of 3D printing of the dual-network conductive Zn metal anode. (b) SEM image of rSA, rSP and rSP/MXene/ZP. (c) Crosslinking mechanism of the rSP hydrogel ionic conductive network. (d) FTIR spectra of rSA, PAAm and rSP and hydrogen bond formation between rSA and Am. (e) BET curves of rSA, rSP and rSP/MXene/ZP. (f) Ionic conductivities of rSP/MXene/ZP, rSP/ZP, rSA/ZP and ZP anodes. (g) 3D snapshot for the rSP/MXene/ZP internal electrolyte system obtained from MD simulation. (h) Zn^{2+} diffusion path in rSP. (i) The function of MSDs *vs.* time in rSA, rSP and Zn-OTf.

As shown in the edge region of the high-resolution TEM (HRTEM) images, the interlayer spacing between two adjacent parallel fringes is about 0.29 nm. Prior to printing, printable inks with desirable rheological properties were formulated and their rheological characteristics were thoroughly evaluated to ensure optimal printability. As shown in Fig. S4a, both the rSP/MXene/ZP and MXene/ZP inks exhibit significant shear-thinning behavior, which facilitates ink extrusion and helps maintain the printed shape. The storage modulus (G') and loss modulus (G'') of the rSP/MXene/ZP and MXene/ZP inks as a function of shear stress are shown in Fig. S4b and c. Both types of electrode inks exhibit a storage modulus greater than the loss modulus near 100 Pa of shear stress, indicative of a solid-like response that is essential for the solidification and shaping of the electrodes. As the shear stress increases, the reduction in the elastic modulus exceeds that of the loss modulus, and the ink adopts a liquid-like behavior. In this regime, the ink predominantly undergoes viscous deformation, which is favorable for the extrusion 3D printing process. The ink exhibits a certain yield stress, which means that it will not flow under a shear stress lower than a specific value. Only when the applied shear stress exceeds the yield stress will the ink begin to flow. This characteristic enables the ink we prepared to remain stationary in a beaker at rest, and it will not flow even when the beaker is inverted (Fig. S4d). Fig. S5 displays scanning electron microscopy (SEM) images of the MXene/ZP anode, where the MXene nanosheets exhibit distinct layered structures that are highly oriented within the electrode. The ZP particles are uniformly distributed between or on the surfaces of the MXene layers. Moreover, the energy dispersive spectroscopy (EDS) maps further demonstrate the uniform distribution of C, Ti, Zn, and O within the printed individual orthogonal layers of the parallel porous cylindrical rods. In addition, the SEM image of the rSP/MXene/ZP anode (Fig. S6) shows that the surface of rSP/MXene/ZP is rich in pores. The formation of this porous structure is likely attributed to the layered arrangement of MXene nanosheets and the cross-linking effect of rSP, which helps to form a stable electrode.

To investigate the influence of different additives on the micro-morphology of the ionic conductive network, SEM was used to examine their microstructures. It was found that the pores in rSA are relatively large, with thick and uneven pore walls. Upon the addition of PAAm, the hydrogel structure becomes denser which indicates enhanced interactions among the components. Further incorporation of MXene and ZP results in more uniform pores with significantly increased pore density, revealing a more densely crosslinked structure, which is beneficial for improving the mechanical strength and electrical conductivity of the hydrogel (Fig. 2b). In addition, the EDS mapping of the rSP/MXene/ZP anode also shows the uniform distribution of C, Ti, O, and Zn, indicating that ZP is evenly distributed in the dual network (Fig. S7). The uniform pores and denser crosslinked structure are mainly attributed to the secondary crosslinking mechanism between rSA and PAAm. As shown in Fig. 2c, the carboxyl groups (–COOH) of rSA and the amide groups (–$CONH_2$) of PAAm can interact through hydrogen bonds to form a crosslinked network. Meanwhile, the excess carboxyl groups of sodium alginate can undergo ionic crosslinking reactions with zinc ions (Zn^{2+}) in the electrolyte. This dual crosslinking mechanism combines the advantages of physical and chemical crosslinking, endowing the hydrogel with greater mechanical strength and stability. As observed in Fig. 2d, in the Fourier-transform infrared (FTIR) spectra, the asymmetric –COO– stretching vibration of rSA at 1594 cm^{-1} shifts to 1595 cm^{-1} after polymerization into rSP, which may be attributed to the interaction between carboxylate ions of rSA and Zn^{2+} in the mixture.[12] The peak associated with the –CO functional group is located at 1026 cm^{-1}. In addition, the hydroxyl group also shifts from 3254 cm^{-1} (rSA) to 3250 cm^{-1} (rSP), indicating that hydrogen bonds are formed between rSA and PAAm after crosslinking.[13] N_2 adsorption/desorption measurements were performed to investigate the surface area of rSA, rSP and rSP/MXene/ZP (Fig. 2e). The adsorption/desorption isotherm of the samples exhibited a type IV profile, indicating that the dual-network ZP anode is predominantly composed of mesopores. Besides, the Barrett–Joyner–Halenda (BJH) pore size distribution of rSP/MXene/ZP further confirms the mesoporous nature (Fig. S8). The N_2 adsorption–desorption analysis showed that the Brunauer–Emmett–Teller (BET) surface areas of rSA, rSP and rSP/MXene/ZP were 105.2, 187.6 and 363.7 $m^2\ g^{-1}$, respectively. The high specific surface area of the network structure exhibits more surface active sites, which can adsorb and dissociate Zn^{2+} in the electrolyte and increase ion concentration and mobility. Mechanical property tests (Fig. S9) revealed that the PAAm hydrogel fractured after rapid stress buildup at 0–400% strain, and the rSP dual-network hydrogel showed superior tensile properties (66.5 kPa strength and 1512% elongation). Additionally, the overall effective ionic conductivities of the samples were measured using the blocking electrode method (Fig. 2f and Fig. S10). ZP exhibited the highest conductivity (65.8 mS cm^{-1}), which is attributed to the interconnected liquid-phase channels formed by the complete filling of interparticle gaps with liquid electrolyte. The lower conductivity of rSA/ZP (11.7 mS cm^{-1}) is mainly ascribed to its rigid structure resulting in insufficient electrolyte retention and higher ion transport tortuosity. The rSP double network, formed by introducing flexible PAAm chains to create an interpenetrating network, enhanced electrolyte retention capacity and reduced effective tortuosity, thereby increasing the effective conductivity to 35.9 mS cm^{-1}. The further introduction of MXene, through its abundant surface oxygen-containing functional groups, promoted uniform electrolyte distribution and interfacial wettability, raising the effective conductivity to 41.2 mS cm^{-1}. Furthermore, the water loss experiments indicate that the ionic conductive network of the crosslinked rSP hydrogel in the rSP/MXene/ZP anode can effectively mitigate the water loss rate compared to the MXene/ZP anode. After pre-soaking the rSP/MXene/ZP anode to a swelling equilibrium state, its water retention rate on the 7th day remains above 70% (Fig. S11). Although the decrease of water reduced the ionic conductivity, the ionic conductivity of rSP/MXene/ZP was still 14.2 mS cm^{-1} after 7 days (Fig. S12). In order to deeply explore the conductive mechanism of the rSP dual-ion conductive network hydrogel, molecular

dynamics (MD) simulation was used to systematically study the diffusion behavior of Zn^{2+} in dual-network carriers (Fig. 2g). The simulation results show that the amide group (–$CONH_2$) in the Am chain interacts with the carboxyl group (–COO^-) in sodium alginate through hydrogen bonds, and a stable ion transport channel is constructed. This hydrogen bond network not only enhances the structural stability of the polymer matrix, but also provides a continuous and less tortuous pathway for ion transport. As shown in Fig. 2h, the transmission path of Zn^{2+} near the dual network clearly shows its rapid migration behavior in the channel. This phenomenon suggests that the synergistic effect of hydrogen bonds and coordination bonds in the dual-network structure facilitates Zn^{2+} migration, thus achieving efficient ion conduction. Time-dependent mean square displacement (MSD) results further validated the diffusion coefficient trend of $Zn(OTf)_2$ electrolyte, rSA, and rSP. Zn^{2+} in $Zn(OTf)_2$ exhibits the greatest diffusion capability due to unconstrained migration in the continuous liquid phase. The rSP double network, through the introduction of flexible PAAm chains, enhances chain mobility and electrolyte retention, forming continuous ion transport channels with reduced tortuosity, resulting in a diffusion coefficient approaching that of the liquid electrolyte. In contrast, the rSA single network shows the lowest diffusion coefficient due to its rigid skeleton, strong cross-linking, and carboxyl–Zn^{2+} coordination confinement that restricts chain rearrangement. This result is consistent with the ionic conductivity measurements, demonstrating that the double-network design can synergistically optimize Zn^{2+} transport by regulating polymer flexibility, electrolyte retention, and the local ion coordination environment (Fig. 2i).

Electrochemical analysis and Zn deposition behavior of the Zn metal anode

To evaluate the advantages of dual-network hydrogel carriers in promoting Zn reversibility, symmetric cells were assembled for a plating/stripping procedure. Furthermore, to optimize the MXene content in the composite anode, rSP/MXene/ZP anodes with different MXene mass fractions (5, 10, 15, 20, and 25 wt%) were fabricated, and their electrochemical performance was systematically compared. As presented in Fig. S13, with MXene contents of 5–25 wt%, the composite electrode impedances are 839.4, 568.6, 380.5, 366.8, and 419.1 Ω, and the Zn anode cycling lifetimes at 10 mA cm^{-2} are 688, 818, 1250, 1102, and 1004 h, respectively. Lower impedance (380.5 Ω) and maximum lifetime (1250 h) at 15 wt% indicate the formation of an optimal continuous conductive network. Fig. 3a and Fig. S14 show the cyclic performance under the condition of 2 mA cm^{-2}/1 mAh cm^{-2}. The lifespans of MXene/ZP and rSP/MXene/ZP symmetric cells are effectively extended, especially for the rSP/MXene/ZP anode with the cycling life of 3000 h, which is almost 12 times that of the bare ZP anode. Moreover, the rSP/MXene/ZP anode remained highly reversible for more than 1200 h of cycling even at a current density of 10 mA cm^{-2} with a capacity of 5 mAh cm^{-2}, which had a low voltage hysteresis of 117 mV (Fig. 3b). In contrast, the bare ZP symmetric cell exhibited intermittent and abrupt drops after 180 h, ultimately leading to an internal short circuit within the cell. Additionally, Zn anodes containing only the rSP ion-conductive network (rSP/ZP) were fabricated and tested (details are provided in Fig. S15), further corroborating that the superior performance of the dual-network architecture stems from the synergistic ionic/electronic dual pathways: the rSP network homogenizes Zn^{2+} flux to suppress dendrite growth, while the MXene network uniformizes local current density and interfacial electric field distribution to alleviate corrosion and guide uniform Zn deposition. The resting and restoring ability of Zn//Zn symmetric cells were further evaluated using the shelving-recovery test (Fig. S16). The bare ZP anode experienced a short circuit after 300 h, whereas the rSP/MXene/ZP anode maintained stable cycling for over 800 h, even after undergoing eight rest-recovery cycles, which suggests that the rSP/MXene/ZP anode exhibits satisfactory structural stability and highly sensitive current response capabilities. To elucidate the enhancing effect of shear-induced directional alignment of MXene nanosheets on zinc dendrite suppression, a cast disordered MXene/ZP anode (denoted as D-MXene/ZP) was simultaneously prepared as a control, and their electrochemical performances were systematically compared (Fig. S17). The cyclic voltammetry (CV) curves (Fig. S18) were also performed to explore the nucleation behavior of Zn^{2+} at the nucleating stage. The nucleation overpotential of rSP/MXene/ZP is slightly higher than that of naked ZP ($|BB_0|$ = 14 mV), which indicates that the conductive dual network causes steric hindrance and reduces the nucleation sites on the Zn surface. Compared with bare Zn, the overpotential is increased by introducing dual networks, which contributes to the refinement of the Zn core. Furthermore, the relationship between the grain radius of Zn (r) and the nucleation overpotential (η) follows the equation:

$$r = 2\frac{\gamma V_m}{F|\eta|}$$

where γ indicates the surface energy of the electrode/electrolyte interface, V_m represents the molar volume of Zn, and F is the Faraday constant. A conductive dual-network hydrogel can reduce the Zn/electrolyte interfacial energy, so the increased nucleation overpotential can further facilitate the formation of smaller nuclei and inhibit dendrite growth. As shown in the Tafel plots (Fig. S19), the corrosion potential of rSP/MXene/ZP is −0.879 V, which is higher than that of MXene/ZP (−0.892 V) and bare ZP (−0.932 V). In addition, the corrosion current density is reduced from 1.37 mA cm^{-2} to 0.104 mA cm^{-2}. These results show that the self-corrosion problem has been effectively alleviated by the dual-network hydrogel protective layer. In addition, linear sweep voltammetry (LSV) was used to study the inhibitory effect of the dual-network hydrogel on the HER at the Zn surface (Fig. 3c). With the gradual addition of MXene and rSP, the potential required to reach 10 mA cm^{-2} shifted from −1.06 V to −1.14 V (*versus* Ag/AgCl), while the cathodic current density remained relatively low. This indicates that the presence of the MXene/rSP dual network can effectively suppress the HER. On the other hand, Fig. 3d shows that the symmetric cell with the rSP/MXene/ZP anode still remains stable as the current density increases from 0.5 mA cm^{-2} to 20 mA cm^{-2}. The voltage hysteresis of rSP/MXene/ZP is always smaller than that of bare ZP. When the

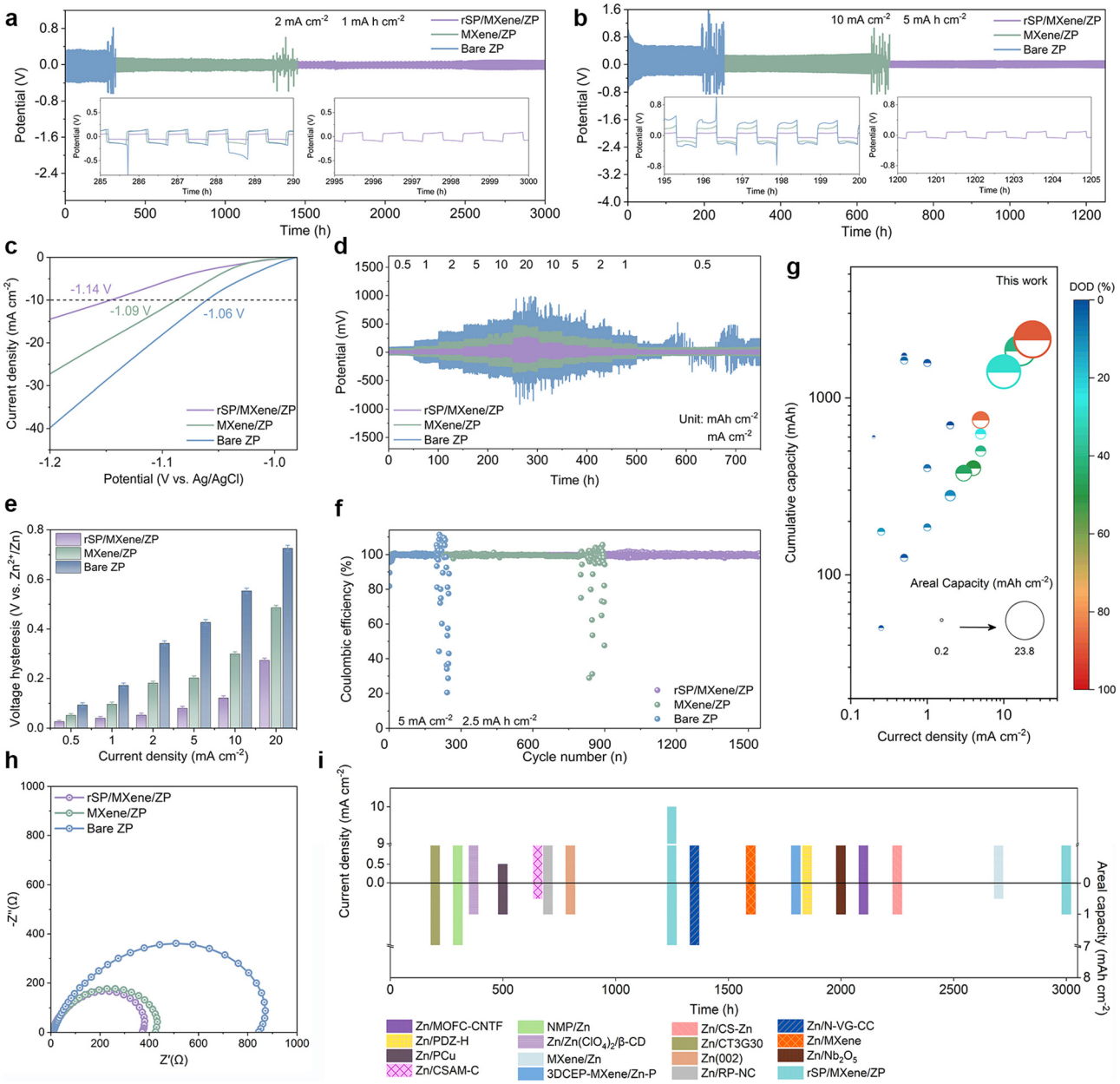

Fig. 3 Investigations of electrochemical properties of various Zn anodes. (a) Voltage profiles of symmetric cells with rSP/MXene/ZP, MXene/ZP, and bare ZP at 2 mA cm^{-2}. (b) Voltage profiles of symmetric cells with rSP/MXene/ZP, MXene/ZP, and bare ZP at current densities of 10 mA cm^{-2}. (c) LSV profiles of rSP/MXene/ZP, MXene/ZP, and bare ZP. (d) Rate performance of symmetric cells with rSP/MXene/ZP, MXene/ZP, and bare ZP anodes. (e) Voltage hysteresis at different current densities from 0.5 to 20 mA cm^{-2}. (f) Coulombic efficiencies of rSP/MXene/ZP, MXene/ZP and bare ZP anodes. (g) Comparison of DOD and cumulative capacity of recently reported Zn//Zn cells with our work.[5,6,12–28] (h) Nyquist plots of rSP/MXene/ZP, MXene/ZP and bare ZP. (i) Lifespan comparison between this work and recently published studies.[6,9,12,13,16,17,20,23,25,29–34]

current increases to 20 mA cm^{-2}, the voltage hysteresis of bare ZP soars to 726 mV due to the aggravation of side reactions, while that of rSP/MXene/ZP is only 273 mV. As for the MXene/ZP anode, it shows a narrow voltage gap, almost the same as rSP/MXene/ZP at low current densities from 0.5 to 10 mA cm^{-2}, but exhibits an even larger voltage hysteresis of 486 mV at 20 mA cm^{-2}. Accordingly, as presented in Fig. 3e, the modified ZP anode shows a lower hysteresis voltage, which is due to the addition of improved conductive dual network rSP/MXene to accelerate the kinetics of Zn^{2+}. In addition, the exchange current density (i_0) associated with the Zn plating process was calculated to accurately assess the deposition kinetics (Fig. S20). The rSP/MXene/ZP anode presents a much lower i_0 of 1.469 mA cm^{-2} compared to that of bare ZP (4.551 mA cm^{-2}), which is usually associated with moderated Zn nucleation and more uniform Zn deposition, thereby reducing dendrite formation and improving the cycling stability of the electrodes. Simultaneously, considering that the reversibility of plating/stripping is crucial for the practical realization of

rechargeable Zn-based devices, the coulombic efficiency (CE) of the anode was also measured. As shown in Fig. 3f, the cell with rSP/MXene/ZP demonstrates a stabilized CE of 99.84% within an ultra-long 1500 h at 5 mA cm^{-2}/2.5 mAh cm^{-2}, but the operating states of MXene/ZP and bare ZP suddenly decay after only 832 and 198 plating/stripping cycles, respectively. Moreover, the charge–discharge voltage profiles from the 1st to the 1500th cycles are shown in Fig. S21. The rSP/MXene/ZP cell exhibits a low plating/stripping voltage hysteresis of 38 mV, which is significantly lower than that of MXene/ZP (51 mV) and bare ZP (131 mV). Compared with the steep tailing observed in the voltage profiles of the bare ZP cells, the voltage profiles of the rSP/MXene/ZP cells remain consistently stable even after the 1500th cycle, indicating that the rSP/MXene ensures uniform Zn deposition and favorable plating/stripping reversibility. Given that DOD is a crucial indicator of the practical applicability of Zn metal anode cells, the DOD of the rSP/MXene/ZP was also assessed. The cycle time of rSP/MXene/ZP anode at 50% DOD and 65% DOD was extended to 450 h and 300 h, respectively, and even under the harsh conditions of 88.5% DOD, it can still maintain stable cycling for 180 h (Fig. S22). To highlight the superior electrochemical properties of the rSP/MXene/ZP symmetrical cells, the cumulative plating capacity was employed as a robust indicator for comparison with previous literature. Obviously, rSP/MXene/ZP supplies a high cumulative plated capacity of 2135 mAh at a current density of 23.72 mA cm^{-2} with 88.5% DOD (Fig. 3g and Table S1), which far exceeds recent state-of-the-art symmetrical Zn//Zn cells.[7,8,14–30] The electrochemical impedance spectroscopy (EIS) curves indicate that the introduction of the MXene conductive network significantly reduced R_{ct} to 425.2 Ω compared with bare ZP (844.5 Ω), which may be attributed to the construction of an internal MXene electronic conductive network that shortens the electron migration distance. The rSP/MXene/ZP anode achieves the lowest practical working impedance (371.8 Ω) through structural stability and interface optimization (Fig. 3h). To evaluate the long-term stability of MXene in the composite electrode, X-ray photoelectron spectroscopy (XPS) characterization of rSP/MXene/ZP before and after cycling was performed. As shown in Fig. S23a and b, Ti predominantly retains its original oxidation states (Ti^{2+}/T^{3+}) in both pristine and cycled samples, with weak Ti^{4+} signals showing no noticeable increase, indicating that MXene avoids significant oxidation during fabrication and cycling. Cross-sectional SEM (Fig. S23c) further reveals that MXene nanosheets maintain an intact lamellar stacking structure without fracture or delamination after long-term cycling. EIS measurement (Fig. S23d) shows that while R_{ct} increases for both electrodes after cycling, rSP/MXene/ZP consistently maintains a lower value (473.6 Ω *vs.* 537.4 Ω for MXene/ZP), confirming that the MXene conductive pathways remain effective and that rSP incorporation enhances interfacial charge transfer stability. As summarized in Fig. 3i and Table S2, the cycling performances compare favorably with those from the symmetric cells enabled by modified ZP and Zn foil anodes, implying the superiority of our dual conductive network hydrogel carrier strategy.[7,11,14,15,18,19,22,25,27,31–36]

To further elucidate the capacity of the rSP/MXene conductive dual-network hydrogel carrier on the Zn plating behavior of ZP, a series of *ex situ* SEM characterizations were performed. The *ex situ* SEM images of the bare ZP anode in Fig. 4a–c show that Zn dendrites began to form on the surface of the bare ZP anode after 50 h, and most of the ZP was completely covered by Zn dendrites after 250 h. As shown in Fig. S24, the directionally arranged MXene conductive network in the MXene/ZP anode can homogenize charge distribution and slightly inhibit dendrite growth, but only delays the growth rate without alleviating the internal stress caused by ZP volume expansion, resulting in obvious cracks after 650 h. In contrast, the rSP/MXene/ZP anode toughened by the rSP hydrogel maintained stable cycling for up to 3000 h. The numerous pores within the anode provided accommodation sites for deposited Zn (Fig. 4d–f). Furthermore, *ex situ* 3D X-ray computed tomography (3DCT) visualization of rSP/MXene/ZP is systematically conducted to gain deep insights into the 3D structure and Zn deposition distribution within the dual-network anode (Fig. 4g). As evident from Fig. 4h, at the initial stage, the pristine rSP/MXene/ZP anode exhibits a dual network structure, where rSP and MXene form an integrated framework (depicted in blue). ZP (depicted in red) are uniformly dispersed within this network (spatial distribution uniformity >90%). After 1500 h of cycling, the deposition of Zn gradually increased, but the overall structure of the electrode remained stable (Fig. 4i). After long-term cycling for 3000 h, the dual-network framework remained intact, although the Zn deposition increased significantly (the volume ratio of the deposited layer increased from 15.4% to 52.7%).

The synergistic effect of the high elastic modulus of rSP and high mechanical strength of MXene provides strong support for the volume change of ZP (Fig. 4j and Fig. S25). Chronoamperometry tests (150 mV) reveal that the bare ZP anode exhibits rapidly increasing current density, indicating uncontrolled 2D planar diffusion and vertical deposition; in contrast, rSP/MXene/ZP achieves stable 3D diffusion-dominated deposition with lower steady-state current due to favorable migration pathways minimizing surface energy (Fig. S26). Online electrochemical mass spectrometry (OEMS) was also employed for the external monitoring of H_2 flux during the Zn plating/stripping process, enabling the accurate quantification of H_2 evolution. As presented in Fig. S27, the bare ZP symmetric cell exhibited a H_2 release rate of 7.36 μmol s^{-1} during 10 h cycles. Surprisingly, the H_2 evolution rate in the rSP/MXene/ZP anode symmetric cell was as low as 1.12 μmol s^{-1}, revealing that the rSP hydrogel network can further suppress the HER. The lowest unoccupied molecular orbital (LUMO) and highest occupied molecular orbital (HOMO) energy levels of the Zn anode are determined by density functional theory (DFT) calculation (Fig. 4k). The results indicate that the LUMO energy levels of Am (−1.03 eV) and rSA (−1.06 eV) in the rSP/MXene/ZP anode are significantly lower than those of H_2O molecules (1.44 eV), suggesting stronger electron-accepting characteristics of the polymer fragments within the dual-network. Therefore, the Am/rSA fragments may participate in interfacial electron redistribution,

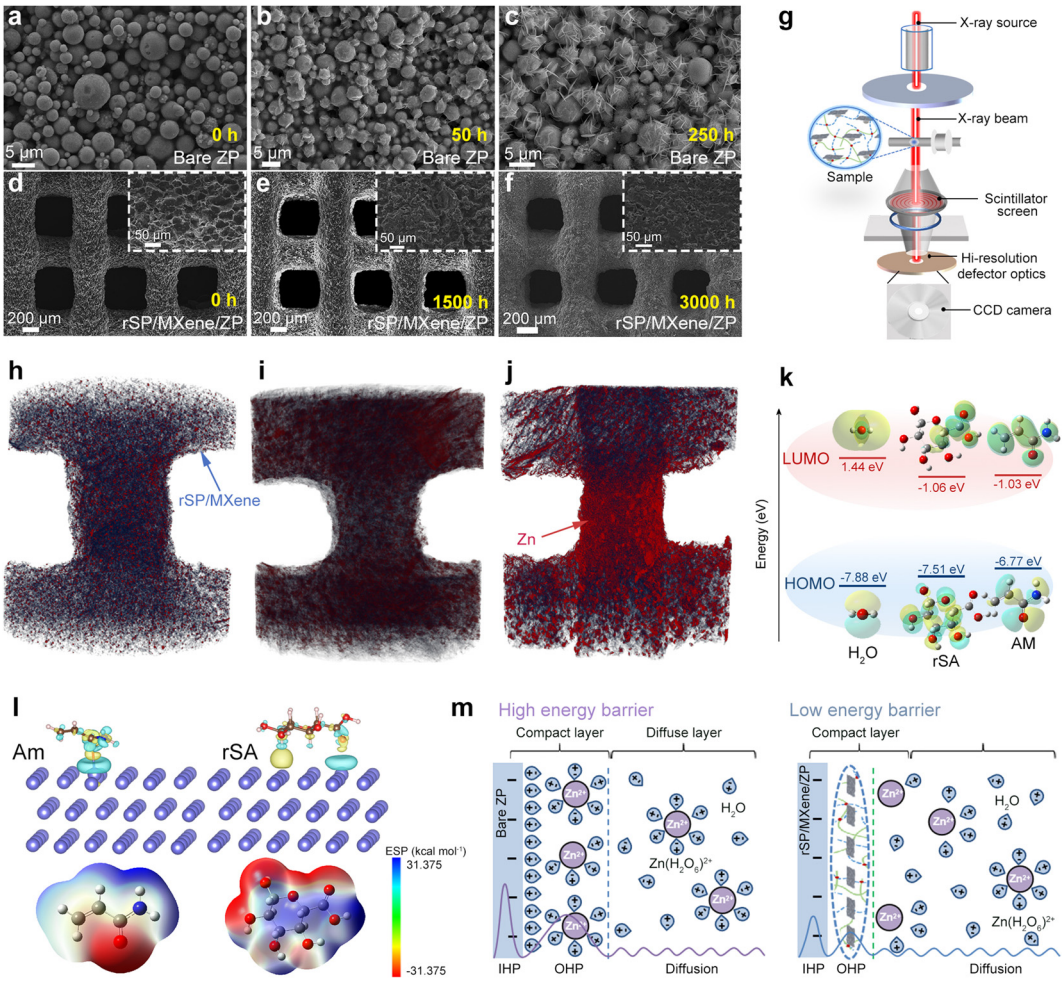

Fig. 4 Investigation of zinc deposition behavior and dendrite suppression mechanism. (a–c) *Ex situ* SEM images of bare ZP and (d–f) rSP/MXene/ZP anodes. (g) Schematic diagram of an X-ray 3D CT facility for the evaluation of bulk phase changes during different cycles. (h–j) *Ex situ* X-ray 3D CT images of the rSP/MXene/ZP anode at different cycling times. (k) Molecular orbital energies of H_2O, rSA, and Am fragments. (l) Charge density difference of the interface between Zn (002) and Am/rSA, ESP of the Am rSP molecule. (m) Schematic of the EDL structure of bare ZP and rSP/MXene/ZP.

which contributes to the suppression of H_2O reduction and the HER. To further explore the mechanism of HER inhibition, the Gibbs free energies of H* adsorption (ΔG_H*) on Zn/Am, Zn/rSA, and bare Zn anodes were calculated. The results showed that the ΔG_H* of the bare Zn anode was 0.69 eV, while the ΔG_H* of Zn/Am and Zn/rSA were 0.92 eV and 0.89 eV, respectively (Fig. S28), indicating that the introduction of rSP significantly increases the H* adsorption free energy, thereby effectively suppressing H* adsorption and reduction. In order to explore the inhibition mechanism of the rSP/MXene dual network on Zn dendrites, DFT calculations were performed to evaluate the adsorption behavior of H_2O, Am, rSA, and an rSP fragment on the Zn(002) surface. The rSP fragment shows a more negative adsorption energy (−1.270 eV) than the individual Am and rSA fragments as well as H_2O, indicating stronger interfacial affinity after considering the combined rSA-Am structure. These results suggest that the rSP network can preferentially interact with the Zn surface and regulate Zn deposition behavior during plating/stripping (Fig. S29).

Charge density difference analysis demonstrates effective modulation of the Helmholtz layer on the Zn surface by the polymer. Besides, the uneven electrostatic potential (ESP) distribution of rSA and Am forms an electrostatic gradient, promoting directional migration of hydrated Zn^{2+} to achieve uniform deposition and suppress dendrite formation (Fig. 4l). To verify the regulating effect of rSP/MXene on the Zn anode electric dual layer, the Arrhenius equation was used to calculate the activation energy (E_a) of Zn^{2+}. The results show that the E_a of bare ZP is 24.7 kJ mol^{-1}, while the E_a of rSP/MXene/ZP is significantly reduced to 13.9 kJ mol^{-1}, which indicates that the introduction of rSP/MXene effectively improves the Helmholtz layer and reduces the energy barrier of Zn^{2+} migration (Fig. S30). According to the Gouy–Chapman–Stern model, the Helmholtz layer at the interface between the anode and the electrolyte is primarily divided into a compact layer and a diffuse layer. The electron transfer process of Zn^{2+} occurs within the compact layer, and the concentration of Zn^{2+}. The potential of the compact layer will affect the activation energy of the electrode reaction through the following formula:[37]

$$j_c = nFK_c c^* \exp(\alpha F(\psi - \psi_1)/RT)$$

where j_c, c^*, ψ, ψ_1, n, F, α, R, T, and K_c represent the reduction rate, concentration of Zn^{2+} in the compact layer, equilibrium potential, potential of the diffusion layer, number of electrons involved in the reaction, Faraday constant, transfer coefficient, molar gas constant, absolute temperature, and reaction rate constant, respectively. Based on this, the construction of the rSP/MXene/ZP dual-network composite anode enhances the potential difference in the compact layer and reduces the activation energy, enabling uniform Zn deposition/stripping. The optimized Helmholtz layer further buffers interfacial stress, reduces side reactions, and improves cycling stability (Fig. 4m).

Construction of the rSP/MXene/ZP//G-PAQS full cell and its Zn^{2+} storage mechanisms

To evaluate practical applications of the rSP/MXene/ZP Zn metal anode, we synthesized the organic polymer poly(2,6-anthraquinone sulfide) (PAQS) and conducted detailed characterizations (details are provided in Fig. S31). Afterwards, PAQS as an organic cathode was coupled with an rSP/MXene/ZP anode to construct full cells (Fig. 5a).

As depicted in Fig. 5b, the rSP/MXene/ZP//G-PAQS demonstrates markedly diminished voltage polarization between redox peaks with enhanced symmetry and sharpness relative to bare ZP//G-PAQS at 2 mV s^{-1}, confirming that the rSP/MXene

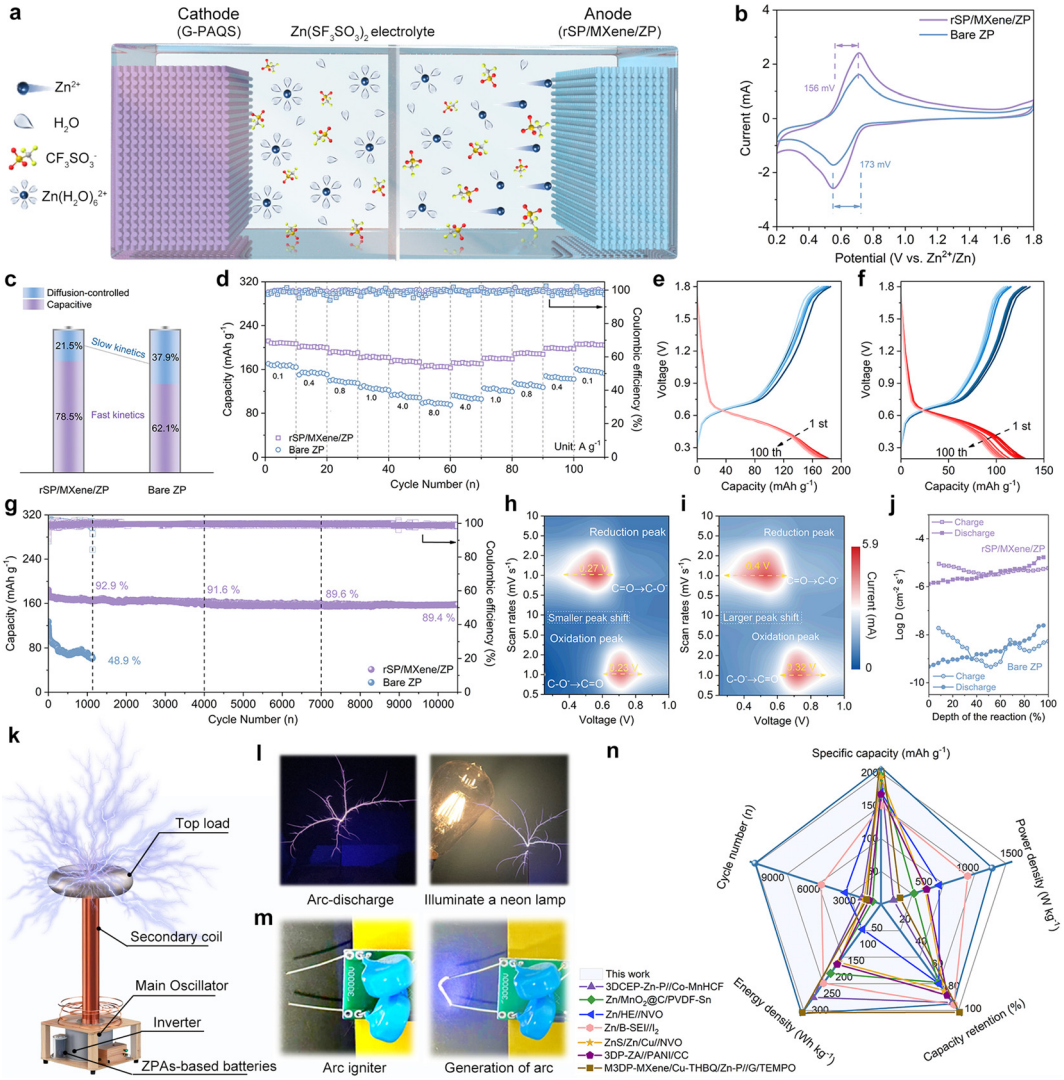

Fig. 5 Electrochemical performance of the rSP/MXene/ZP//G-PAQS Zn-ion full cell. (a) Working principle of the rSP/MXene/ZP//G-PAQS full cell. (b) CV curves and (c) contribution ratio of rSP/MXene/ZP//G-PAQS and bare ZP//G-PAQS full cells. (d) Rate performance of rSP/MXene/ZP//G-PAQS and bare ZP//G-PAQS full cells. (e and f) Charge and discharge curves of different samples at different numbers of cycles. (g) Cycling stability of different full cells with anodes. (h) Contour plots of CV patterns for rSP/MXene/ZP and (i) bare ZP under different scan rates. (j) Zn^{2+} diffusion coefficients (DZn^{2+}) of rSP/MXene/ZP//G-PAQS and bare ZP//G-PAQS full cells. (k) Schematic diagram of miniaturized Tesla coil. (l) Optical diagram of cell-powered Tesla coil and (m) arc igniter concept presentation. (n) Comparison of the comprehensive performance of the rSP/MXene/ZP full cell with the performances that have been reported for other Zn^{2+} cells.

efficiently mitigates parasitic reactions and promotes charge transfer reversibility. Fig. 5c exhibits capacitive contribution ratios at a scan rate of 2 mV s^{-1}, and the capacitive contribution of the rSP/MXene/ZP//G-PAQS full cell is 78.5%, which is higher than that of bare ZP//G-PAQS. This result further indicates that the addition of rSP/MXene significantly reduces the charge transfer impedance of the electrode and promotes the rapid charge transfer. As depicted in Fig. 5d and Fig. S32, the rSP/MXene/ZP//G-PAQS full cell achieves a high discharge capacity of 208.2 mAh g^{-1} at 0.1 A g^{-1}, with specific capacities of 202.4, 192.3, 182.1, 176.6, and 166.8 mAh g^{-1} maintained at current densities of 0.4, 0.8, 1.0, 4.0, and 8.0 A g^{-1}, respectively. The discharge curves of the full cell with the rSP/MXene/ZP anode over 100 cycles shows the higher initial capacity and narrow-range distribution compared to the full cell with bare ZP, which indicates that it has remarkable working stability (Fig. 5e and f). Surprisingly, rSP/MXene/ZP//G-PAQS has ultrahigh cycling stability compared with bare ZP//G-PAQS at a current density of 4 A g^{-1} (Fig. 5g), and the capacity retention rate after 1134 cycles is 92.9%, which is much higher than that of bare ZP//G-PAQS (48.9%). After 4000 cycles, the capacity retention rate slowly decreased to 91.6%, and finally decreased to 92.4% after 10 560 cycles. Furthermore, the *b*-values and capacity contributions ratio were calculated based on the peak current and scan rate of CV curves. It is worth noting that the *b*-values of peak 1 and peak 2 are 0.83 and 0.81, respectively, indicating that the reactions represented by these peaks are predominantly controlled by capacitive behavior (Fig. S33 and S34). In addition, as the scan rate of the CV curves increased from 0.5 to 10 mV s^{-1}, the capacitive contribution ratio of the rSP/MXene/ZP//G-PAQS full cell eventually rose to 89.2%, indicating that the electrode material exhibited higher pseudocapacitive characteristics during the electrochemical reaction process, enabling faster charge transfer rates and higher power densities (Fig. S35). The CV contour plots reveal that rSP/MXene/ZP//G-PAQS exhibits narrower peak widths, higher current responses, and smaller peak shifts compared to bare ZP//G-PAQS, indicating faster reaction kinetics and lower voltage polarization (Fig. 5h and i). The diffusion of Zn^{2+} in full cells with different anodes were quantified by a galvanostatic intermittence titration technique (GITT). As shown in Fig. 5j and Fig. S36, the calculated diffusion coefficient of Zn^{2+} is as high as $\sim 10^{-5}$ cm^2 s^{-1}, which is better than that of 10^{-8}–10^{-9} of bare ZP//G-PAQS. This further elucidates the reasons for the high performance of the rSP/MXene/ZP//G-PAQS full cell. To demonstrate the practical applicability of the rSP/MXene/ZP//G-PAQS full cell, we assembled a miniaturized Tesla coil, as shown in Fig. 5k, serving as a conceptual demonstration of portable wireless transmission technology. The mini-Tesla coil consists of a top load, primary oscillator, inverter, secondary coil, and a Zn-ion cell pack. The 8 V cell pack is assembled by five rSP/MXene/ZP//G-PAQS full cells (Fig. S37). The cell pack connects to a custom inverter that converts DC into high-frequency AC. When activated, the primary coil generates an alternating magnetic field, inducing high voltage in the multi-turn secondary coil. The increased voltage strengthens the electric field, ionizing air to produce corona discharge and exciting gas molecules in the neon tube to illuminate. This process validates the Tesla coil principle and demonstrates the practical value of the cell pack as a DC power source (Fig. 5l and Movie S1). Additionally, the DC from the cell pack can be converted into high voltage through the built-in boost circuit of the arc igniter, ionizing air to generate an arc between the electrodes for rapid and reliable ignition of combustion equipment (Fig. 5m). Overall, compared with the comprehensive performance of most aqueous Zn-ion cells reported previously, the rSP/MXene/ZP//G-PAQS Zn metal anode-based Zn-ion cell exhibits a satisfactory discharge capacity of 208.2 mAh g^{-1}, high energy density of 333.1 Wh kg^{-1}, remarkable power density of 1270.9 W kg^{-1}, and excellent cycling stability (a capacity retention rate of 92.4% after 10 560 cycles), which demonstrates the superiority of the Zn metal anode-based cell and its great potential as a next-generation energy storage device (Fig. 5n and Table S3).[7,11,14,23,32,38–47]

To further investigate the reaction mechanisms of the rSP/MXene/ZP//G-PAQS full cell, we also conducted a series of *ex situ* and *in situ* characterizations. The chemical bonds in G-PAQS were systematically analyzed by FTIR spectroscopy, revealing the dynamic changes of chemical bonds during charging and discharging. In the *in situ* FTIR spectrum of PAQS (Fig. 6a), the intensity of the carbonyl group (C═O) decreased at 1673 cm^{-1} after the initial discharge to 0.2 V. Concurrently, a new band appeared at 1303 cm^{-1}, which was mainly due to the C–O stretching vibration of the enol functional group (C–O^-), indicating that carbonyl group (C═O) was transformed into the enol group (C–O^-) through tautomerism. In addition, due to the existence of a conjugated system (such as an aromatic ring or conjugated dual bond), the strength of the C–O bond may be enhanced, and the absorption peak position may be further pushed up. Subsequently, upon recharging from 0.2 V to 1.8 V, the intensity of the carbonyl (C═O) peak recovers, while the enol group peak gradually fades away. In the final discharge process, the intensity of the carbonyl (C═O) peak diminishes once more, and the enol group (C–O^-) peak reappears, demonstrating the reversibility of the C═O and C–O^- conversion process. Moreover, *ex situ* XPS Zn 2p spectra reveal the reversible uptake of Zn^{2+} during the discharge process and its deintercalation after charging (Fig. 6b). It is worth noting that in the pristine state, no Zn 2p signal was detected in PAQS, indicating the absence of Zn^{2+} in the PAQS material under initial conditions. However, in the fully discharged state, characteristic peaks of Zn $2p_{1/2}$ and Zn $2p_{3/2}$ were observed, indicating the successful adsorption of Zn^{2+} by the PAQS cathode. As the full cell was charged to 1.8 V, the intensity of these characteristic peaks decreased, reflecting the desorption of Zn^{2+} from the PAQS cathode. This phenomenon further confirms the adsorption and desorption behavior of Zn^{2+} by PAQS during the electrochemical cycling. As shown in Fig. 6c, C 1s spectra could be split into three peaks, assigned to the bonds of C–C (284.7 eV), C–S/C–O (285.4 eV) as well as C═O (287 eV), respectively. The C–C bonds in the anthraquinone structure

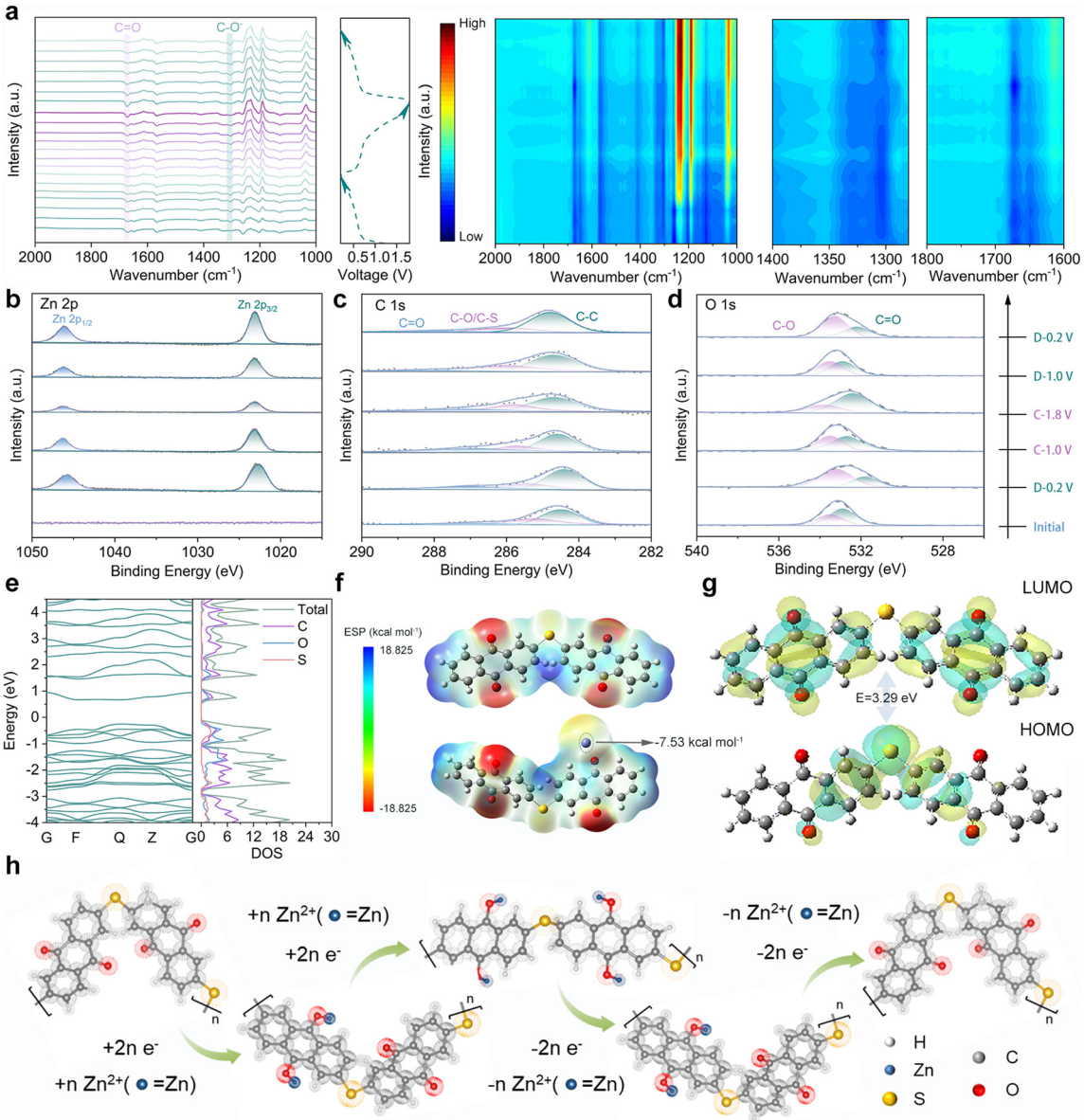

Fig. 6 Investigation of the Zn^{2+} storage mechanism. (a) *In situ* FTIR of the rSP/MXene/ZP//G-PAQS full battery at various voltages. *Ex situ* high-resolution XPS spectra of (b) Zn 2p, (c) C 1s and (d) O 1s at different charge–discharge statuses. (e) Calculated band structure and PDOS for PAQS. (f) ESP images of PAQS and Zn^{2+} coordination with PAQS. (g) LUMO and HOMO of PAQS. (h) Reversible Zn^{2+} storage mechanism of the rSP/MXene/ZP//G-PAQS full cell during the charging and discharging process.

remain unchanged throughout the entire charging and discharging process, indicating the high structural stability of the PAQS conjugated framework. In addition, throughout the entire charging and discharging process of the cell, there is a slight tendency for interconversion between the C═O and C–O/C–S bonds. In contrast, obvious changes are observed in the O spectra (Fig. 6d). Compared to the initial state, the C═O peak (532.6 eV) of PAQS significantly decreases during the discharge process, while the C–O peak (533.4 eV) markedly increases, consistent with the enolization mechanism. In the charged state, the C═O peak increases and the C–O peak decreases, indicating the high redox reversibility of PAQS.

The reversible capacity is generally consistent with the changes in the intensity of the C═O/C–O peaks. To deeply understand the electronic structure of PAQS, the density of states (DOS) of PAQS are shown in Fig. 6e. PAQS has a calculated band gap of 0.92 eV, indicating that it is a narrow-band-gap semiconductor. This narrow band gap suggests a relatively low energy requirement for electronic excitation from the valence band to the conduction band. The ESP image of PAQS shows the electrostatic potential distribution in various regions of the PAQS molecular surface. Obviously, the red area indicates the negative charge concentration area, and the C–O site is the main active site for Zn^{2+} storage, and its negative potential is strong, which is beneficial to the adsorption of Zn^{2+}

(Fig. 6f). Besides, the LUMO value of the PAQS molecule is −3.25 eV, and the HOMO value is −6.54 eV, indicating a favorable affinity toward cation coordination. The HOMO–LUMO gap of 3.29 eV suggests accessible frontier orbitals for redox reactions, which may facilitate interfacial electron transfer and redox kinetics. These characteristics further confirm the good performance of PAQS in electrochemical cycling (Fig. 6g). The reaction mechanism could be expressed in Fig. 6h, the electrochemical behavior of PAQS during charging and discharging is based on the reversible redox reaction of the anthraquinone unit, which involves the conversion between carbonyl C=O and C–O$^-$ after enolization. During the discharge process, PAQS accepts electrons and embeds Zn^{2+} to form a reduced complex; when charged, the complex releases electrons and deintercalates Zn^{2+}, and returns to its initial state.

Closed-loop recovery and sustainable utilization of the rSP/MXene/ZP Zn metal anode

Recycling of the Zn metal anode in ZIBs is not only a necessary measure for resource conservation and environmental protection, but also an important way to promote technological progress and

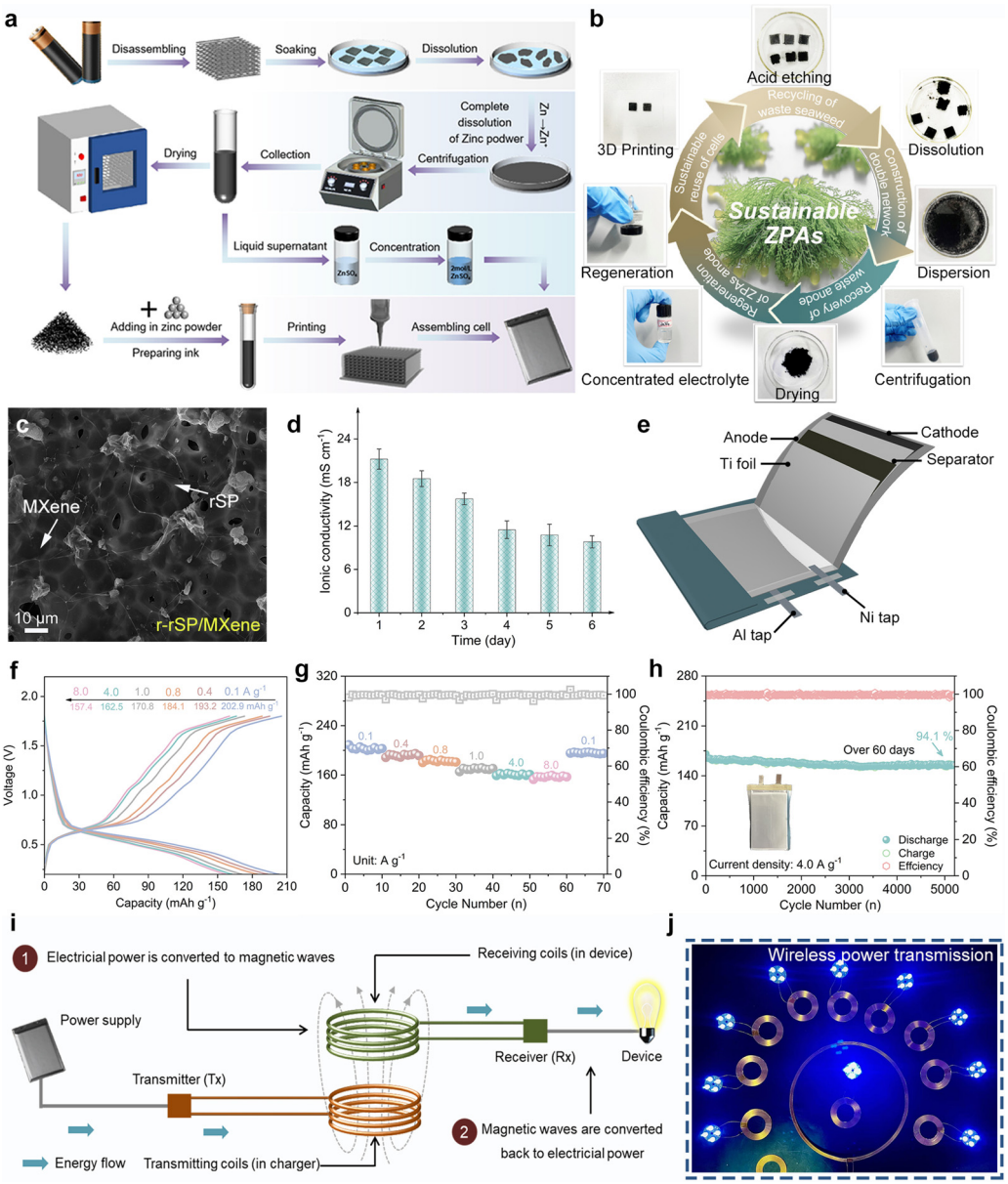

Fig. 7 Recovery and regeneration of the rSP/MXene/ZP Zn metal anode. (a) Schematic diagram of wet recovery of the rSP/MXene/ZP anode. (b) Optical diagram of the rSP/MXene/ZP actual recovery process. (c) SEM image of the r-rSP/MXene dual network carrier. (d) Ion conductivity of the r-rSP/MXene dual network carrier after being placed for different times. (e) Schematic diagram of the r-rSP/MXene/ZP assembled pouch cell. (f) GCD curves, (g) rate performance and (h) cyclic performance of the r-rSP/MXene/ZP//G-PAQS pouch cell. (i) Cell-powered wireless power transmission technology based on magnetic induction. (j) Optical photos of energy conversion of the r-rSP/MXene/ZP//G-PAQS pouch cell pack *via* a magnetic induction coil.

achieve sustainable development. In this study, we employed a wet recycling process for the treatment of used and discarded rSP/MXene/ZP anodes. Initially, a grinding and acid leaching method was utilized to remove the Zn deposits, simultaneously separating the MXene/SP dual-network carrier. Subsequently, the recovered rSP/MXene (r-rSP/MXene) was subjected to centrifugation and drying to facilitate its reuse. Notably, Zn deposits that react with dilute H_2SO_4 are converted into $ZnSO_4$, which can be used as regenerated electrolyte after concentration. The regeneration process of the Zn anode mainly involves mixing the recovered rSP/MXene dual-network carrier with ZP to prepare printable inks, and then printed into an electrode again (Fig. 7a and b). The SEM image of the r-rSP/MXene dual-network carrier is shown in Fig. 7c. Although it is recycled after use, its internal dual-network structure remains intact, and the rSP ionic conductive framework and the MXene layer on its surface can be clearly observed. The regenerated cell employs recycled $ZnSO_4$ as the electrolyte to verify the full closed-loop utilization of zinc components (including anode zinc powder and deposits) within the recovery system, demonstrating that by-products can also be converted into functional electrolyte. Furthermore, the r-rSP/MXene dual-network carrier was soaked in recycled $ZnSO_4$ to test its ionic conductivity at different time intervals. The initial ionic conductivity was measured to be 21.27 mS cm^{-1}. After being left in air for six days, the ionic conductivity decreased to 9.82 mS cm^{-1} (Fig. 7d). Due to the satisfactory ionic conductivity of the dual network carrier hydrogel, the r-rSP/MXene/ZP Zn anode can still achieve highly stable cycling for 1000 h at a current density of 2 mA cm^{-2} with a limited capacity of 1 mAh cm^{-2}. Furthermore, the r-rSP/MXene/ZP anode paired with $Zn(OTf)_2$ electrolyte achieves a cycling life of 1872 h, indicating that the regeneration-induced structural damage accounts for approximately 37.6% of the lifespan decay, while the insulating by-product deposits formed by SO_4^{2-} in the $ZnSO_4$ electrolyte disrupt interfacial uniformity and contribute an additional ~29% degradation (Fig. S38). To further verify the practical applicability of the r-rSP/MXene/ZP anode, we assembled pouch cells by directly printing r-rSP/MXene/ZP anode inks and G-PAQS cathode inks onto current collectors and using recycled 2 M $ZnSO_4$ as the electrolyte. We then proceeded to test the electrochemical properties of the pouch full cells (Fig. 7e). Impressively, the r-rSP/MXene/ZP//G-PAQS full cell provides desirable reversible capacities of 202.9, 193.2, 184.1, 170.8 and 162.5 mAh g^{-1} at different current densities of 0.1, 0.4, 0.8, 1 and 4 A g^{-1}, respectively. And its capacity retention rate is still 77.6% of its initial capacity even at a high current density of 8 A g^{-1} (Fig. 7f and g). Furthermore, the r-rSP/MXene/ZP//G-PAQS full cell demonstrates exceptional cycling stability (Fig. 7h), retaining a high capacity retention rate of 94.1% even after 5220 cycles (over 60 days). In order to further verify the reliability of the pouch full cell in practical application, we assembled it into a cell pack by series and parallel connection. As illustrated in Fig. 7i, battery-powered magnetic induction wireless power transfer technology combines portability with wireless energy transmission, providing flexible and efficient energy solutions for mobile devices, wearables, and electric vehicles. As a proof of concept, DC from the r-rSP/MXene/ZP//G-PAQS cell is converted into high-frequency AC by an inverter and fed into the transmitting coil to generate an alternating magnetic field; the receiving coil induces current through electromagnetic induction, which is rectified to drive a bulb, achieving wireless energy transfer *via* magnetic coupling (Fig. 7j and Movie S2).

Conclusion

Inspired by the hierarchical network structure of large ampulla dragline silk, we have designed a dual-network hydrogel carrier that integrates both flexibility and rigidity. This biomimetic design successfully demonstrates the core application value of renewable biomass in energy storage devices with bioinspired architectures. It is found that a polymer network with high ionic conductivity is obtained by transforming and crosslinking the biomass alginate polymer in waste algae. Simultaneously, by combining it with an MXene conductive network, the green and high-stability Zn metal anode was directly manufactured *via* multi-band UV 3D printing integrated technology. This achievement proves the feasibility of the disposable green biomaterials in the application of high-performance energy storage. Benefiting from the high ionic conduction channel constructed by the dual-network conductive hydrogel carrier, the rSP/MXene/ZP anode can achieve good compatibility with organic cathode materials. After more than 10 560 cycles, their impressive performance shows that they are expected to be candidates for low-cost and high-safety green energy storage devices. Meanwhile, the integration of series–parallel full batteries with a miniature Tesla coil demonstrates wireless power transmission without physical connections, offering a novel solution for powering portable devices. More surprisingly, this bionic dual-network Zn metal anode can be recycled in a sustainable closed loop, and the regenerated electrode still maintains satisfactory electrochemical performance. These findings provide a feasible paradigm for the development of next generation energy storage devices with high safety and environmental friendliness.

Conflicts of interest

The authors declare no conflicts of interest.

Data availability

All data supporting the findings of this study are included in the article and its supplementary information (SI). Supplementary information is available. See DOI: https://doi.org/10.1039/d6ee02022d.

Acknowledgements

H. L., B. X., J. Z. and G. S. acknowledge the support from The Research Grants Council of Hong Kong (RGC Junior Research

Fellowship Scheme, Grant No.: JRFS2526-5S06), the National Natural Science Foundation of China (523B2019), The Hong Kong Polytechnic University (PolyU Distinguished Postdoctoral Fellowship Scheme, Grant No.: 4-YWER) and the start-up grant of Sichuan Agricultural University (031-2122996035). G. Y. acknowledges the support from the Welch Foundation Award F-1861.

Notes and references

1 J. Li, S. Li, J. Huang, A. Q. Khan, B. An, X. Zhou, Z. Liu and M. Zhu, *Adv. Sci.*, 2022, **9**, 2103965.
2 J. J. Hug, D. Krug and R. Müller, *Nat. Rev. Chem.*, 2020, **4**, 172–193.
3 A. Rising and J. Johansson, *Nat. Chem. Biol.*, 2015, **11**, 309–315.
4 Z. Liu, F. Feng, W. Feng, G. Wang, B. Qi, M. Gong, F. Zhang and H. Pang, *Energy Environ. Sci.*, 2025, **18**, 3568–3613.
5 A. Li, Z. Xu, S. W. Lo, X. Zhang, H. Jiang and M. Wu, *Adv. Funct. Mater.*, 2026, **36**, e18964.
6 K. Song, B. Yang, Q. Liang, W. An, J. Yu, Z. Chu, F. Liu, Z. Jiang, B. Xu, W. Li, W. Zhang and W. Zheng, *Sci. Bull.*, 2025, **70**, 634–637.
7 H. Lu, J. Hu, Y. Zhang, K. Zhang, X. Yan, H. Li, J. Li, Y. Li, J. Zhao and B. Xu, *Adv. Mater.*, 2023, **35**, 2209886.
8 M. Zhang, P. Yu, K. Xiong, Y. Wang, Y. Liu and Y. Liang, *Adv. Mater.*, 2022, **34**, 2200860.
9 Q. Hu, J. Hu, F. Ma, Y. Liu, L. Xu, L. Li, S. Zhang, X. Liu, J. Zhao and H. Pang, *Energy Environ. Sci.*, 2024, **17**, 2554–2565.
10 Z. Shao, L. Lin, W. Zhuang, S. Liu, P. Yang, K. Zhu, C. Li, G. Guo, W. Wang, Q. Zhang and Y. Yao, *Adv. Mater.*, 2024, **36**, 2406093.
11 H. Lu, J. Hu, K. Zhang, J. Zhao, S. Deng, Y. Li, B. Xu and H. Pang, *Adv. Mater.*, 2024, **36**, 2309753.
12 B. Zhang, L. Qin, Y. Fang, Y. Chai, X. Xie, B. Lu, S. Liang and J. Zhou, *Sci. Bull.*, 2022, **67**, 955–962.
13 D. Ji, J. M. Park, M. S. Oh, T. L. Nguyen, H. Shin, J. S. Kim, D. Kim, H. S. Park and J. Kim, *Nat. Commun.*, 2022, **13**, 3019.
14 Y. Gao, N. Yang, F. Bu, Q. Cao, J. Pu, Y. Wang, T. Meng, J. Chen, W. Zhao and C. Guan, *Energy Environ. Sci.*, 2024, **17**, 1894–1903.
15 H. Yu, Y. Zeng, N. W. Li, D. Luan, L. Yu and X. W. D. Lou, *Sci. Adv.*, 2022, **8**, eabm5766.
16 Q. Zhang, J. Luan, X. Huang, Q. Wang, D. Sun, Y. Tang, X. Ji and H. Wang, *Nat. Commun.*, 2020, **11**, 3961.
17 H. Lu, J. Hu, X. Wei, K. Zhang, X. Xiao, J. Zhao, Q. Hu, J. Yu, G. Zhou and B. Xu, *Nat. Commun.*, 2023, **14**, 4435.
18 G. Zhang, X. Zhang, H. Liu, J. Li, Y. Chen and H. Duan, *Adv. Energy Mater.*, 2021, **11**, 2003927.
19 H. Lu, J. Hu, L. Wang, J. Li, X. Ma, Z. Zhu, H. Li, Y. Zhao, Y. Li, J. Zhao and B. Xu, *Adv. Funct. Mater.*, 2022, **32**, 2112540.
20 P. X. Sun, Z. Cao, Y. X. Zeng, W. W. Xie, N. W. Li, D. Luan, S. Yang, L. Yu and X. W. D. Lou, *Angew. Chem., Int. Ed.*, 2022, **61**, e202115649.
21 Y. Li, W. Li, K. Li, W. Jiang, Y. Tang, X. Zhang, H. Yuan, J. Zhang and X. Wu, *J. Am. Chem. Soc.*, 2024, **146**, 30998–31011.
22 L. Hong, X. Wu, L. Wang, M. Zhong, P. Zhang, L. Jiang, W. Huang, Y. Wang, K. Wang and J. Chen, *ACS Nano*, 2022, **16**, 6906–6915.
23 Z. Shen, L. Luo, C. Li, J. Pu, J. Xie, L. Wang, Z. Huai, Z. Dai, Y. Yao and G. Hong, *Adv. Energy Mater.*, 2021, **11**, 2100214.
24 Y. Zeng, P. X. Sun, Z. Pei, Q. Jin, X. Zhang, L. Yu and X. W. D. Lou, *Adv. Mater.*, 2022, **34**, 2200342.
25 Q. Cao, Z. Pan, Y. Gao, J. Pu, G. Fu, G. Cheng and C. Guan, *Adv. Funct. Mater.*, 2022, **32**, 2205771.
26 J. Zhu, M. Yang, Y. Hu, M. Yao, J. Chen and Z. Niu, *Adv. Mater.*, 2024, **36**, 2304426.
27 Y. Yang, C. Liu, Z. Lv, H. Yang, Y. Zhang, M. Ye, L. Chen, J. Zhao and C. C. Li, *Adv. Mater.*, 2021, **33**, 2007388.
28 M. Li, X. Wang, J. Hu, J. Zhu, C. Niu, H. Zhang, C. Li, B. Wu, C. Han and L. Mai, *Angew. Chem., Int. Ed.*, 2023, **62**, e202215552.
29 D. Lee, H. Kim, W. Kim, S. Cho, K. Baek, K. Jeong, D. B. Ahn, S. Park, S. J. Kang and S. Lee, *Adv. Funct. Mater.*, 2021, **31**, 2103850.
30 Z. Shao, L. Lin, W. Zhuang, S. Liu, P. Yang, K. Zhu, C. Li, G. Guo, W. Wang, Q. Zhang and Y. Yao, *Adv. Mater.*, 2024, **36**, 2406093.
31 M. Wang, Z. Dai, C. Yang, D. Xu, X. Zhang, L. Que, X. Zhang and J. Qin, *Mater. Today Energy*, 2024, **46**, 101736.
32 Y. Meng, M. Wang, J. Wang, X. Huang, X. Zhou, M. Sajid, Z. Xie, R. Luo, Z. Zhu, Z. Zhang, N. A. Khan, Y. Wang, Z. Li and W. Chen, *Nat. Commun.*, 2024, **15**, 8431.
33 Z. Zheng, X. Zhong, Q. Zhang, M. Zhang, L. Dai, X. Xiao, J. Xu, M. Jiao, B. Wang, H. Li, Y. Jia, R. Mao and G. Zhou, *Nat. Commun.*, 2024, **15**, 753.
34 N. Yang, Y. Gao, F. Bu, Q. Cao, J. Yang, J. Cui, Y. Wang, J. Chen, X. Liu and C. Guan, *Adv. Mater.*, 2024, **36**, 2312934.
35 Y. Zhou, J. Xia, J. Di, Z. Sun, L. Zhao, L. Li, Y. Wu, L. Dong, X. Wang and Q. Li, *Adv. Energy Mater.*, 2023, **13**, 2203165.
36 S. Zhao, X. Liu, T. Chang, H. Tang, T. Tian, Q. Weng and T. Liu, *Energy Storage Mater.*, 2024, **72**, 103769.
37 R. Liu, Y. Cui, L. Liu and F. Wang, *Acta Mater.*, 2021, **203**, 116467.
38 Q. Cao, Y. Gao, J. Pu, X. Zhao, Y. Wang, J. Chen and C. Guan, *Nat. Commun.*, 2023, **14**, 641.
39 Y. Wang, Z. Wang, W. K. Pang, W. Lie, J. A. Yuwono, G. Liang, S. Liu, A. M. D. Angelo, J. Deng, Y. Fan, K. Davey, B. Li and Z. Guo, *Nat. Commun.*, 2023, **14**, 2720.
40 L. Zeng, J. He, C. Yang, D. Luo, H. Yu, H. He and C. Zhang, *Energy Storage Mater.*, 2023, **54**, 469–477.
41 W. Deng, Z. Li, Y. Ye, Z. Zhou, Y. Li, M. Zhang, X. Yuan, J. Hu, W. Zhao, Z. Huang, C. Li, H. Chen, J. Zheng and R. Li, *Adv. Energy Mater.*, 2021, **11**, 2003639.
42 K. W. Nam, S. S. Park, R. Dos Reis, V. P. Dravid, H. Kim, C. A. Mirkin and J. F. Stoddart, *Nat. Commun.*, 2019, **10**, 4948.
43 J. Wu, Q. Kuang, K. Zhang, J. Feng, C. Huang, J. Li, Q. Fan, Y. Dong and Y. Zhao, *Energy Storage Mater.*, 2021, **41**, 297–309.

44 L. Ma, S. Chen, C. Long, X. Li, Y. Zhao, Z. Liu, Z. Huang, B. Dong, J. A. Zapien and C. Zhi, *Adv. Energy Mater.*, 2019, **9**, 1902446.
45 J. Zhou, F. Wu, Y. Mei, Y. Hao, L. Li, M. Xie and R. Chen, *Adv. Mater.*, 2022, **34**, 2200782.
46 Y. Dong, S. Di, F. Zhang, X. Bian, Y. Wang, J. Xu, L. Wang, F. Cheng and N. Zhang, *J. Mater. Chem. A*, 2020, **8**, 3252–3261.
47 M. Idrees, S. Batool, J. Cao, M. S. Javed, S. Xiong, C. Liu and Z. Chen, *Nano Energy*, 2022, **100**, 107505.

